Lab on a Chip

Supplementary Information

Title: Passive droplet trafficking at microfluidic junctions with geometric and flow asymmetries

Authors: Tomasz Glawdel, Caglar Elbuken, Carolyn L. Ren

S.1 General Case Discrete Model

For the general case the critical transition from filtering to sorting is:

$$\frac{2}{\lambda^*} = floor\left[\frac{\left(R_{hyd}^* - P^*\right)}{P^* R_{drop}^{*(a)}}\right] + 1 \tag{1}$$

Replacing $\Lambda^* = T_b^* \beta^* / \left(T_a^* A^*\right)$ and $\frac{2}{\lambda^*}\frac{A^{*(a)}}{\beta^{*(a)}} = T_a^*$, the new discrete calculation for the total number of droplets becomes:

$$N_T = ceil\left[T_a^* \Lambda_{dis}^* \frac{\left(1 + \frac{P^*}{R_{drop}^*}\right)}{\left(\Lambda_{dis}^* + \frac{P^* \beta^*}{R_{drop}^* A^*}\right)} - \frac{\left(R_{hyd}^* - P^*\right)}{R_{drop}^{*(a)} R_{drop}^* A^*} \frac{\left(\Lambda_{dis}^* A^* - \beta^*\right)}{\left(\Lambda_{dis}^* + \frac{P^* \beta^*}{R_{drop}^* A^*}\right)}\right] \tag{2}$$

and the base value for N_b is:

$$N_b = ceil\left[\frac{P^*}{P^* + R_{drop}^*}\left(N_T - \frac{\left(R_{hyd}^* - P^*\right)}{P^* R_{drop}^{*(a)}}\right)\right] \tag{3}$$

These values for N_T and N_b are then used in the calculation of the selection rules.

S.2 Flow Chart for Selection Rules

The algorithm is summarized in the flow chart presented in Figure S.1. To be clear the overall step by step process is outlined below:

(1) Calculate an estimate for N_T and N_b

(2) Calculate the 4 ψ.'s.

(3) Calculate $Ch_{1\text{-}3}$ and then the cycle time inequality

(4) Follow the algorithm to determine the predicted case and obtain the results.

Note that if there is no solution found the algorithm returns a pattern length of 0.

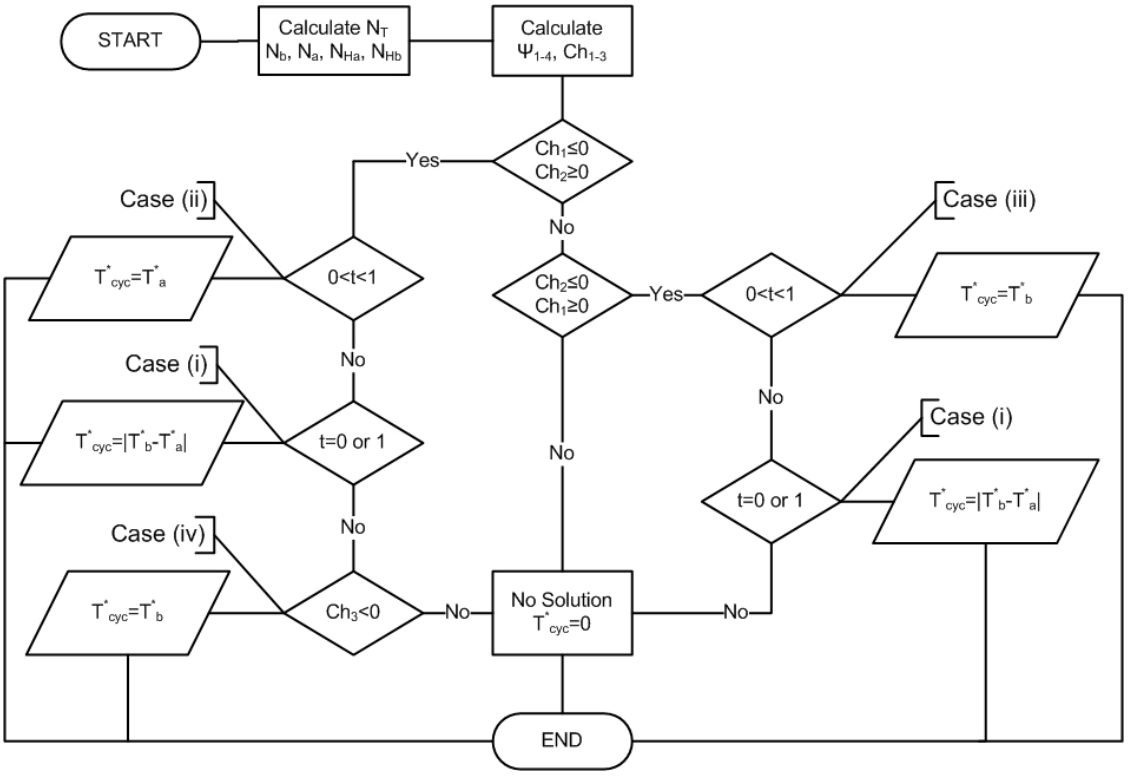

Fig S.1 Flow chart of the selection rule algorithm for the new discrete model.

S.3 Calculating Unique Sequences

To demonstrate the method of determining the number of unique sequences a short example is provided for a pattern length of 6. The first step is to calculate the Cyclic Index, $Z(C_p)$, for the Cyclic Group, C_p, which is given as:

$$Z(C_p) = \frac{1}{p}\sum_{k|p}\varphi(k)a_k^{p/k} \tag{5}$$

where k|p means k *divides* p for integers, and $\varphi(k)$ is Euler's Totient function. For $T^*_{cyc}=6$:

$$Z(C_6) = \frac{1}{6}\left(a_1^6 + a_2^3 + 2a_3^2 + 2a_6^1\right) \tag{6}$$

The notation $a_k^{p/k}$ refers to the cycle structure representation. For droplet sorting, the cycle structure consists of 2 unknowns (*U, D*) and has the form of *(x+y)*, if there were 3 choices the structure is the form of *(x+y+z)* and so on. Substitution of the following terms: $a_1^6 = (x+y)^6$, $a_2^3 = (x^2+y^2)^3$, $a_3^2 = (x^3+y^3)^2$, $a_6^1 = (x^6+y^6)$ results in:

$$Z(C_p) = \frac{1}{6}\left((x+y)^6 + (x^2+y^2)^3 + 2(x^3+y^3)^2 + 2(x^6+y^6)\right) \tag{7}$$

The number of unique patterns for a specific combination, say 4 U-s and 2 D-s, is determined by calculating the coefficient for the term x^4y^2,where *x* corresponds to *U* and *y* to *D*. Expanding Eqn. (7) and grouping the terms can be tedious, instead the calculation may be expedited by using the formula for multinomial coefficients:

$$(x+y)^n = \sum_{\substack{i+j=n \\ i,j\geq 0}} \frac{n!}{i!\,j!}x^i y^j \tag{8}$$

For x^4y^2, only $(x+y)^6$ and $(x^2+y^2)^3$ can produce x^4y^2 and using Eqn 8 the multinomial coefficients are $\frac{6!}{4!2!}$ and $\frac{3!}{2!1!}$, resulting in a total coefficient of $\frac{1}{6}\left(\frac{6!}{4!2!}+\frac{3!}{2!1!}\right)=3$. Thus there are a total of 3 unique patterns for 4 U-s 2 D-s. Table S.1 summarizes the calculation for pattern lengths 2 through 9, including the specific sequences that can be obtained. The usefulness of Póyla's becomes apparent as the length of the pattern increases. A pattern length of 10, for instance, has 5 unique patterns with 2 D-s, 22 with 3 D-s and 26 with 4 D-s.

Table S.1. List of all unique sequences $|\Omega_{seq}|$ that are possible for T^*_{cyc}= *2 to 9* with the number of D-s in the sequence varying from 1-4.

T^*_{cyc}	$Z(C_p)$	$\|\Omega_{seq}\|$ 1 D-s	$\|\Omega_{seq}\|$ 2 D-s	$\|\Omega_{seq}\|$ 3 D-s	$\|\Omega_{seq}\|$ 4 D-s
2	$\frac{1}{2}\left(a_1^2 + a_2^1\right)$	1 [UD]	--	--	--
3	$\frac{1}{3}\left(a_1^3 + 2a_3^1\right)$	1 [UUD]	--	--	--
4	$\frac{1}{4}\left(a_1^4 + a_2^2 + 2a_4^1\right)$	1 [UUUD]	2 [UUDD] [UDUD]	--	--
5	$\frac{1}{5}\left(a_1^5 + 4a_5^1\right)$	1 [UUUUD]	2 [UUUDD] [UUDUD]	--	--
6	$\frac{1}{6}\left(a_1^6 + a_2^3 + 2a_3^2 + 2a_6^1\right)$	1 [UUUUUD]	3 [UUUUDD] [UUUDUD] [UUDUUD]	4 [UUUDDD] [UDUDUD] [UUDUDD] [UUDDUD]	--
7	$\frac{1}{7}\left(a_1^7 + 6a_7^1\right)$	1 [UUUUUUD]	3 [UUUUUDD] [UUUUDUD] [UUUDUUD]	5 [UUUUDDD] [UUDUDUD] [UUUDUDD] [UDUUUDD] [UUDUUDD]	--
8	$\frac{1}{8}\left(a_1^8 + a_2^4 + 2a_4^2 + 4a_8^1\right)$	1 [UUUUUUUD]	4 [UUUUUUDD] [UUUUUDUD] [UUUUDUUD] [UUUDUUUD]	7 [UUUUUDDD] [UUUDUDUD] [UUUUDUDD] [UUDUUDUD] [UUUDUUDD] [UUDUUUDD] [UDUUUUDD]	10 [UUUUDDDD] [UUDDUUDD] [UUUDUDDD] [UDDUUUDD] [UUDUUDDD] [UUDUDUDD] [UDUUUDDD] [UDUUDUDD] [UUUDDUDD] [UDUDUDUD]
9	$\frac{1}{9}\left(a_1^9 + 2a_3^3 + 6a_9^1\right)$	1 [UUUUUUUD]	4 [UUUUUUUDD] [UUUUUUDUD] [UUUUUDUUD] [UUUUDUUUD]	10 [UUUUUUDDD] [UDUUUUUDD] [UUUUUDUDD] [UUUUDUDUD] [UUUUDUUDD] [UUUDUUDUD] [UUUDUUUDD] [UUDUUUDUD] [UUDUUUUDD] [UUDUUDUUD]	14 [UUUUUDDDD] [UUUDUDUDD] [UUUUDUDDD] [UUDUDUUDD] [UUUDUUDDD] [UUDUUDUDD] [UUDUUUDDD] [UDUUUDUDD] [UDUUUUDDD] [UDUUDUUDD] [UUUUDDUDD] [UDUDUUUDD] [UUUDDUUDD] [UUDUDUDUD]

S.4 Experimental Procedure

To observe stable sorting at the junction requires very stable experimental conditions or sorting patterns will quickly disintegrate once they form. The major contributions to instability include: [1-2]

- Sudden pressure fluctuations from droplets forming, sorting or exiting a channel.
- Pressure fluctuates from the regulators.
- Variation in droplet resistance from variations in size and speed of droplets.
- Variation in droplet spacing which can alter the cycle time of the branches
- Delay in sorting at the junction due to stagnation of the droplet as it makes its decision.

When performing trafficking experiments researchers have tackled these issues in a variety of ways. The goal in the design is to isolate the sorting junction form the rest of the network. This requires high resistance channels to be placed between the various components to reduce fluctuation in flow rates caused by dynamically changing hydrodynamic resistances within the network. In the current study, the problem is more complicated because the pressure at the outlets needs to be controlled unlike previous works which used a closed loop system to study the sorting phenomena. In addition, we use a passive droplet generator technique so that coupling between the various components must be kept to a minimum.

S.4.1 Overall Chip Design

The chip consists of three main components: (1) T-junction generator where droplets are formed which then connects to (2) the diluter that controls and increases the spacing and speed of droplets by adding more oil to the flow and (3) the sorting branches and recombination loop as shown in Figure S2. Two sorting channel configurations were tested in the experiments, a symmetric design (5, 5 mm) and an asymmetric design (4, 5mm). Compact fluid flow modeling was used to design the overall network to suppress the influence of the noise factors discussed above. Variance was purposely added to each microchannel in the form of one droplet leaving or exiting and the fluctuations in flow rate through the network were analyzed. Figure 1b shows the equivalent compact model network used in the analysis. The final dimensions for the network are summarized in Table 3.3.

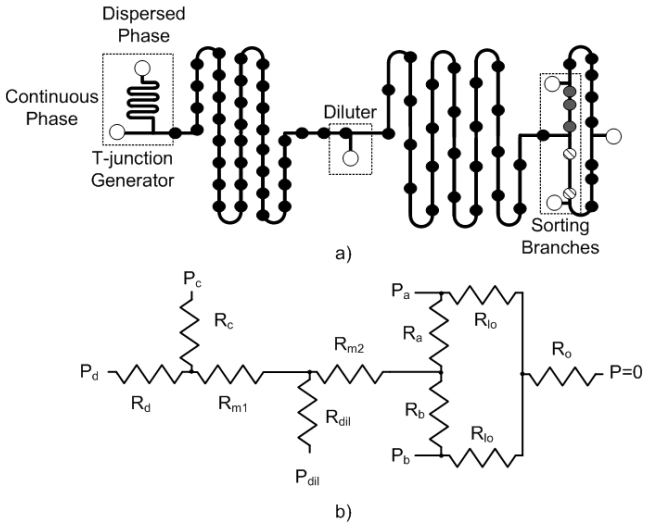

Fig. S2 (a) Overall network architecture for the experimental sorting chip which consists of 3 main components: the T-junction generator, diluter and sorting branches. (b) The equivalent hydrodynamic representation of the network used for compact flow modelling. Pressure skew is added by varying P_a and P_b.

Table S2. Dimensions of the final chip design. Data includes the overall length of the channel and the approximate number of droplets for a typical spacing of 600 µm. The cross-sectional area of all the channels was 50x100µm.

Channel	Description	Length (mm)	Approx. # of Droplets	Notes
R_d	Dispersed Phase Inlet	5	--	
R_c	Continuous Phase Inlet	300	--	Large serpentine channel
R_{m1}	Main outlet for T-junction	50	80	Serpentine radius 2mm
R_{m2}	Main outlet for Diluter	100	165	Serpentine radius 2mm
R_{dil}	Diluter Inlet	0.5	--	Very short
R_a	Sorting Branch a	4,5	15	Small exit to the outlet
R_b	Sorting Branch b	5	15	Small exit to the outlet
R_{lo}	Loop Branch	20	50	
R_o	Outlet of System	4	---	Special guided exit

The channel after the diluter was designed to be very long compared to the sorting branches so that oscillations in the resistance of the branches would have negligible influence on the dilution. The inlet of the diluter was extremely short to reduce pressure losses between the tubing and the microchannel (see Figure S3a). Initial designs did not include a recombination loop after the sorting branches and droplets would exit from the end of the sorting branches. This caused several problems with regards to sorting. As droplets entered the reservoirs they would expand uncontrollably which caused large pressure fluctuations due to the changing Laplace pressure across the droplet. This would create a sudden pressure pulse that would disturb sorting at the junction. Furthermore, once droplets entered the reservoir they sometimes became trapped and would occasionally block the exit causing further oscillations in the pressure field. To overcome this problem the recombination loop was added and a positive flow was applied from the sorting outlets to propel droplets forward. Now as the droplets exit the branching channels additional oil from P_a and P_b increases the spacing of the droplets. Droplets exit the network through a single outlet that has a special designed track to guide droplets away from the exit of the channel (see Figure S3c).

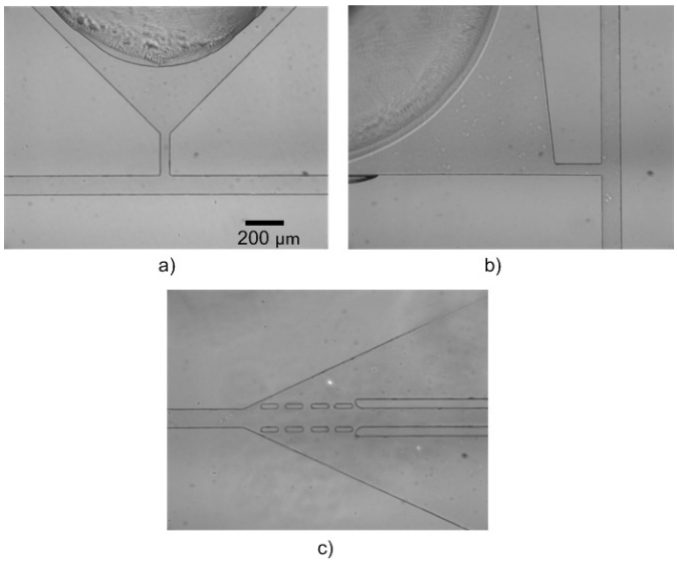

Fig. S3 Micrographs of the chip near (a) the diluter inlet, (b) the outlet of the branches and (c) the exit of the chip. At each inlet drop of glue was added to the master to create a large reservoir that minimized pressure losses from the inlet tubing to the microchannel.

Figure S4 shows the experimental results under the final design and experimental conditions. The figure presents the time trace spacing for four different measurements using the same chip. Measurements were made for approximately 80 pairs of droplets which is approximately one complete volume replacement of the main channel. Standard deviations for these results ranged from 1-1.5% of the mean value with min and max values of 2.5-3%. This is comparable to the experimental variance in experiments by Sessoms *et al.*[2] Variance greater than 2% usually resulted in no discernable pattern formation above pattern lengths of 4.

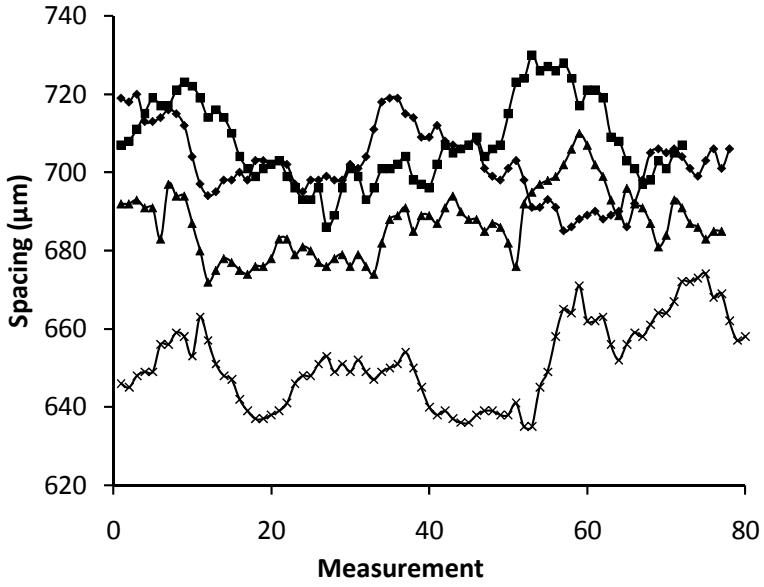

Fig. S4 Droplet spacing measured over 80 droplets for 4 different cases using the same chip.

S4.2 Chip Fabrication

Briefly, two SU-8 masters were fabricated for the experiments with channel heights of 50µm for the 5:5 mm and 5:4 mm designs. PDMS molds with a base to curing agent ratio of 5:1 were made from these masters which were subsequently oxygen plasma bonded (500mTorr, 29.7W for 20s) to PDMS coated glass slides. A lower ratio of PDMS base to curing agent creates a stiffer material that is able to withstand swelling and bulging better. Completed chips were then heated overnight at 160˚C to allow the PDMS to revert back to its natural hydrophobic nature. Prior to beginning experiments, silicone oil was pumped through the network for 45min to allow the channels to swell completely and to achieve proper wetting of the oil with PDMS.

S4.3 Data Extraction from Videos

During an experiment a chip is mounted in an inverted epifluorescence microscope system (Eclipse Ti, Nikon) connected to a CCD camera. Fluids are controlled using a high precision microfluidic pressure control system that operates up to 1bar (MFSC 8C, Fluigent). Figure S5 shows a typical image captured by the camera during the sorting experiments. Images that are captured are analyzed using a custom program developed in Matlab (Mathworks, Inc.). Two detection boxes are drawn on top of the outlet channels and a passing interface is detected by a change in the overall intensity. Using the phase contrast on the microscope causes the rounded interface of the droplet to be significantly brighter than the surrounding oil which allows for straightforward detection of the droplets.

Pressures are adjusted upstream at the T-junction generator (P_c, P_d) and diluter (P_{dil}) to control the size and spacing of incoming droplets. Pressure skew at the sorting junction is controlled by adjusting P_a and P_b (refer to Figure S2). Once settings are in place the system is allowed to reach steady state (~15min) before videos are taken of the sorting process at the junction.

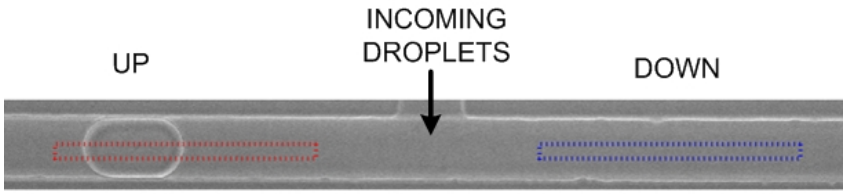

Fig. S5 Snapshot from a video of the sorting process with the two interrogation boxes overlaid.

For each measurement at least 100 sorting events are analyzed and the trajectory of each droplet is recorded as a string of characters. An algorithm adapted from Smith and Gaver is then applied to extract a pattern. [3] The algorithm creates a stencil of potential pattern length *n* from the first *n* events and compares it to the remaining sequence. If the stencil repeats for the entire sequence then the pattern is said to be converged. If not, then the stencil length is increased and the process repeats. If no pattern is found over the entire length of the sequence then the sorting is assumed to be chaotic. Note that this method finds the smallest pattern length, which may be a harmonic of a longer overall pattern. For example, the alternating sequence of UDUDUDUD, will result in a pattern length of 2 (UD) but the entire pattern is actually a multiple of this harmonic.

In addition to extracting the sorting pattern the incoming and outgoing frequency and spacing of the droplets are calculated. The speed and size of the droplets are measured beforehand by analyzing a high speed video of the incoming droplets. The incoming spacing is then calculated by the frequency of incoming droplets and the speed ($\lambda=u/f$). The fraction of droplets sorting into the two channels is determined as the portion of U and D events from the total sequence.

S.4.4 Measuring Droplet Resistance Experimentally

Several factors influence the hydrodynamic resistance of a droplet train including (a) the Laplace pressure drop across the front and back caps, (b) viscous dissipation in the thin film surrounding the droplets, (c) the continuous phase bypassing the droplets through the gutters (d) viscous dissipation from eddies created in the continuous phase and within the droplets. [4-6] To compare the experimental results with the theoretical predictions accurate measurements of the droplet resistance are needed.

Experiments were performed using the same design as for the sorting experiments except that outlets B and C were plugged so that droplets formed upstream at the T-junction only exit outlet A (see Figure S6). The pressure drop across the outlet channel (from the diluting inlet to the exit) was measured by assuming that the pressure at the diluting inlet was the same as the pressure which was applied. The flow rate was measured using a flow sensor (Senserion SLG-1430) connected in series at outlet A. The flow sensor was calibrated for silicon oil beforehand using a syringe pump. Before running the chip with the droplets, the channel resistance without droplets was measured for 3 different pressures (500, 800, 1000 mbar) to quantify any bulging effects. Typically, the channel resistance would change by 10% from 500 to 1000 mbar. A curve fit was applied to the data in order to estimate the natural channel resistance at an applied pressure when performing the droplet resistance calculations.

Droplets of various size, spacing and speeds were generated using the T-junction generator and the pressure drop and flow rate were recorded, for various combinations of silicone oil and water/glycerol. The droplet resistance was calculated using the following equation:

$$R_{drop} = \frac{R^{+}_{hyd} - R_{hyd}}{n} \qquad (9)$$

R^{+}_{hyd} is the hydrodynamic resistance of the channel with droplets, R_{hyd} without droplets, n is the total number of droplets in channel as measured from the spacing.

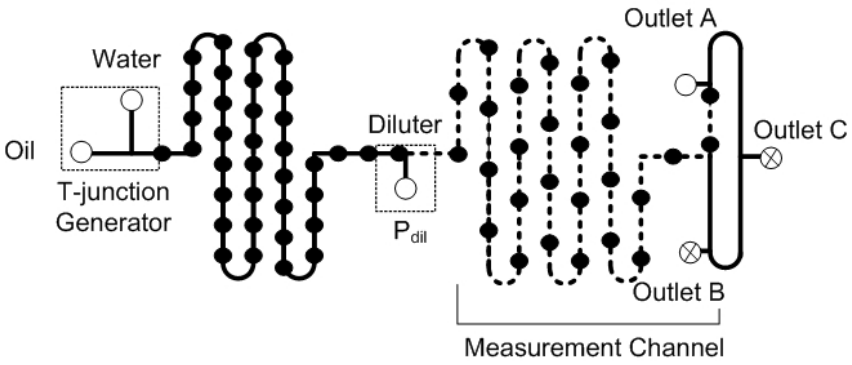

Fig. S6 Modified chip design for the droplet measurement using the applied pressure at the diluter (P_{dil}) and the resistance of the measurement channel (dashed line). The flow sensor is connected to Outlet A, while Outlets B and C are plugged during the measurements. Droplet spacing and speed is measured at the bifurcation using the high speed camera.

Experiments were performed with two water/oil combinations: water/silicone oil and 60%glycerol+water/silicone oil. Surfactants were present in both cases (1% SDS in the aqueous solution). Measurements were made for various droplet sizes under typical flow conditions in the sorting experiments (*Ca~0.005*). The results are presented in Figure S7. In both cases, droplet resistance increased proportionally with droplet length in the measurement range. As well, the glycerol/water combination resulted in twice the droplet resistance for the same size.

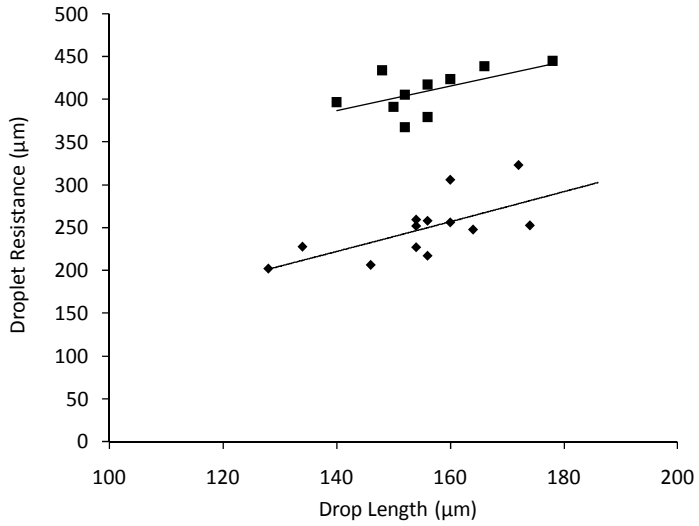

Fig. S7 Equivalent droplet resistance L_{Rdrop} with respect to droplet length L_d for μ^*=0.1 (♦) and μ^*=1(■). Trend lines are linear fits to the data.

S5 Additional Model Comparisons

In the following sections additional validations are provided for the theoretical model and the numerical results.

S5.1 Model Comparison General Case

Four example studies were preformed for several types of asymmetries as summarized in Table S3.

Table S3 Six case studies for the general numerical simulations. Parameters include the length of the two branches (L_1, L_2) [mm], pressures (P_1, P_2) [Pa], droplet equivalent lengths (L_{drop1}, L_{drop2}) [mm], widths and height (w,h) [μm] and relative slip (β_1, β_2). The dimensionless variables are the area ratio A^*, droplet resistance ratio R^*_{drop}, branch length ratio Λ and pressure skew P^*. Pressure at the junction was set to 100 Pa.

Case	L_1	L_2	P_1	P_2	L_{drop1}	L_{drop2}	w,h_1	w,h_2	A^*	R^*_{drop}	Λ^*	P^*	β^*
1	5	4.5	10	0	0.5	0.5	100,50	80,50	0.8	1	0.9	1.11	1
2	5	4	0	10	0.5	1	100,50	80,50	0.8	2	0.8	0.9	1
3	5	5	0	20	0.5	0.25	100,50	80,50	0.8	0.5	1	0.8	1
4	5	5	0	10	0.5	0.25	100,50	100,50	1	0.5	1	0.9	1
5	5	5	0	0	0.25	0.25	100,50	100,50	1	1	1	1	1.2
6	5	4.5	0	20	0.25	0.25	100,50	100,50	1	1	0.9	0.8	1.2

Results for the pattern length (i.e. T^*_{cyc}) are presented in Figure S8, and for the probability of a droplet sorting into branch b ($Prob_b$) in Figure S9 for the first four cases. Results for the last two cases involving differences in slip are presented in Figures S10 and S11. The discrete model is able to accurately predict the limit of the filtering regime and shows a significant improvement over the continuum model prediction. In these four cases, the numbers of droplets needed to balance the system (N_{bal}) are 2, 3, 8, and 2 respectively. As predicted, cycle times correspond either to T^*_a or T^*_b and transitions from one regime to another are accurately predicted by the model. Overall the distribution of droplets into channel b increases, although not monotonically, and approaches an asymptote at higher values of $2/\lambda^*$. This limit extends to the continuum approximation as the population of droplets in the channels increases. The figures clearly show that the oscillations are well described by the discrete model predictions. Most of the plateaus are captured by the model as well as the discontinuous jumps in the distribution as periodic regimes are crossed. Additionally, the critical transition from filtering to sorting is accurately predicted.

Over the 46 cases considered here the sequence length was predicted correctly 93.6% of the time. This result is skewed by Case #2, where the accuracy was only 56.4%. Poor predictions are typically caused by a poor estimation of N_T . Generally, there is a slight over prediction for n_T . This becomes a problem near whole numbers where a small over estimation causes the ceiling function to set N_T to the wrong value (+1 of the actual) during the calculations. This is due to the large number of variables combined with the problems of discretizing the calculations. In the following section the discrete model is compared to more practical conditions with only asymmetric pressures and branch lengths, and the lower number of variables leads to improved accuracy.

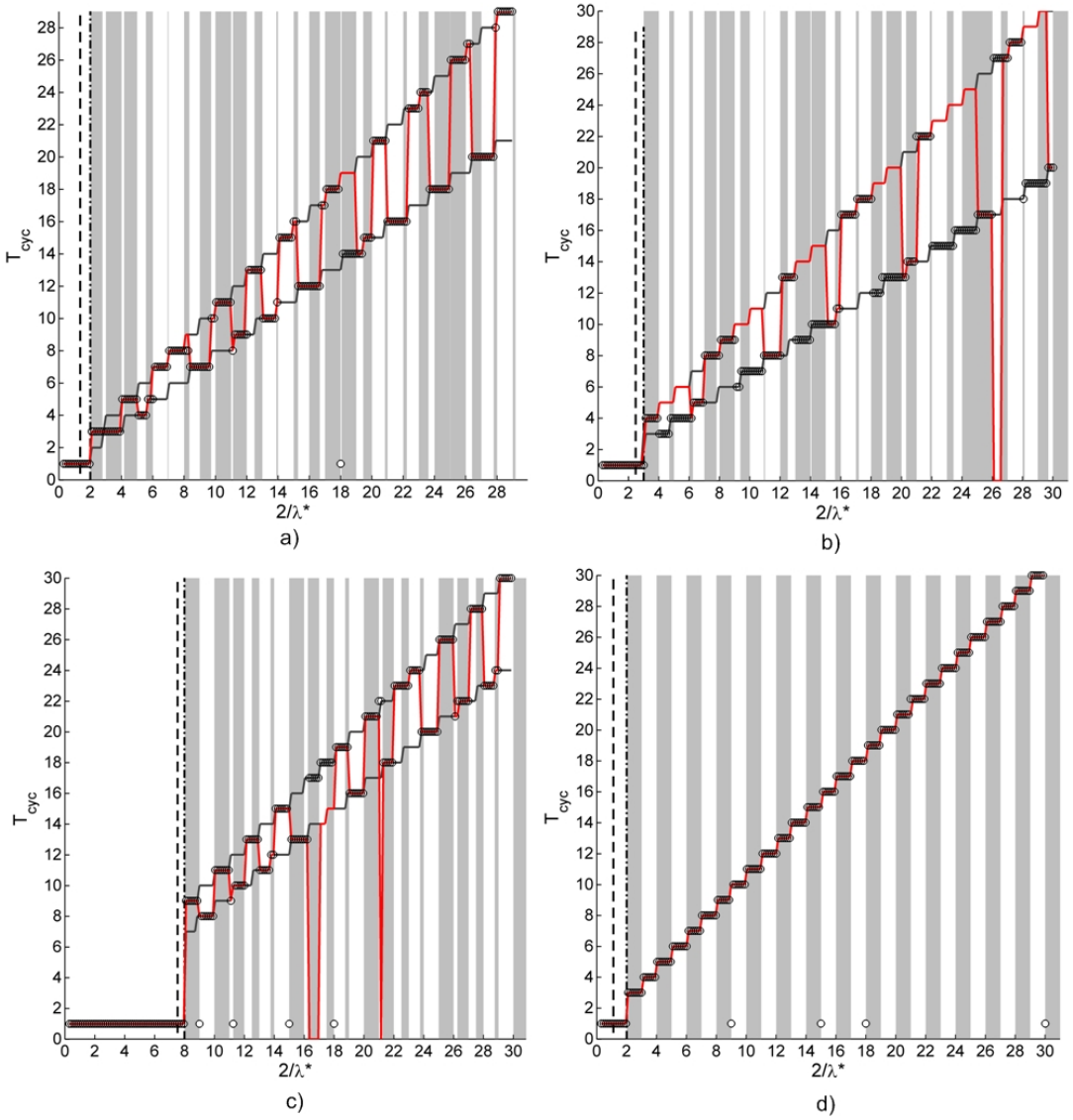

Fig.S8 Idealized numerical simulation results for the pattern length (○). Overlaid are the predictions from the continuum and discrete models. Vertical dashed lines on the left represent the limits for the filtering regime as predicted by the continuum (--) and discrete models (·–). Grey and white regions define the regions where the cycle time is expected to remain unchanged. Black lines are the predictions for T^*_a and T^*_b from the discrete model. The red line corresponds to the selection rules derived in the manuscript. Each plot corresponds to Case 1(a), Case2 (b), Case 3(c) and Case 4 (d) form Table S3.

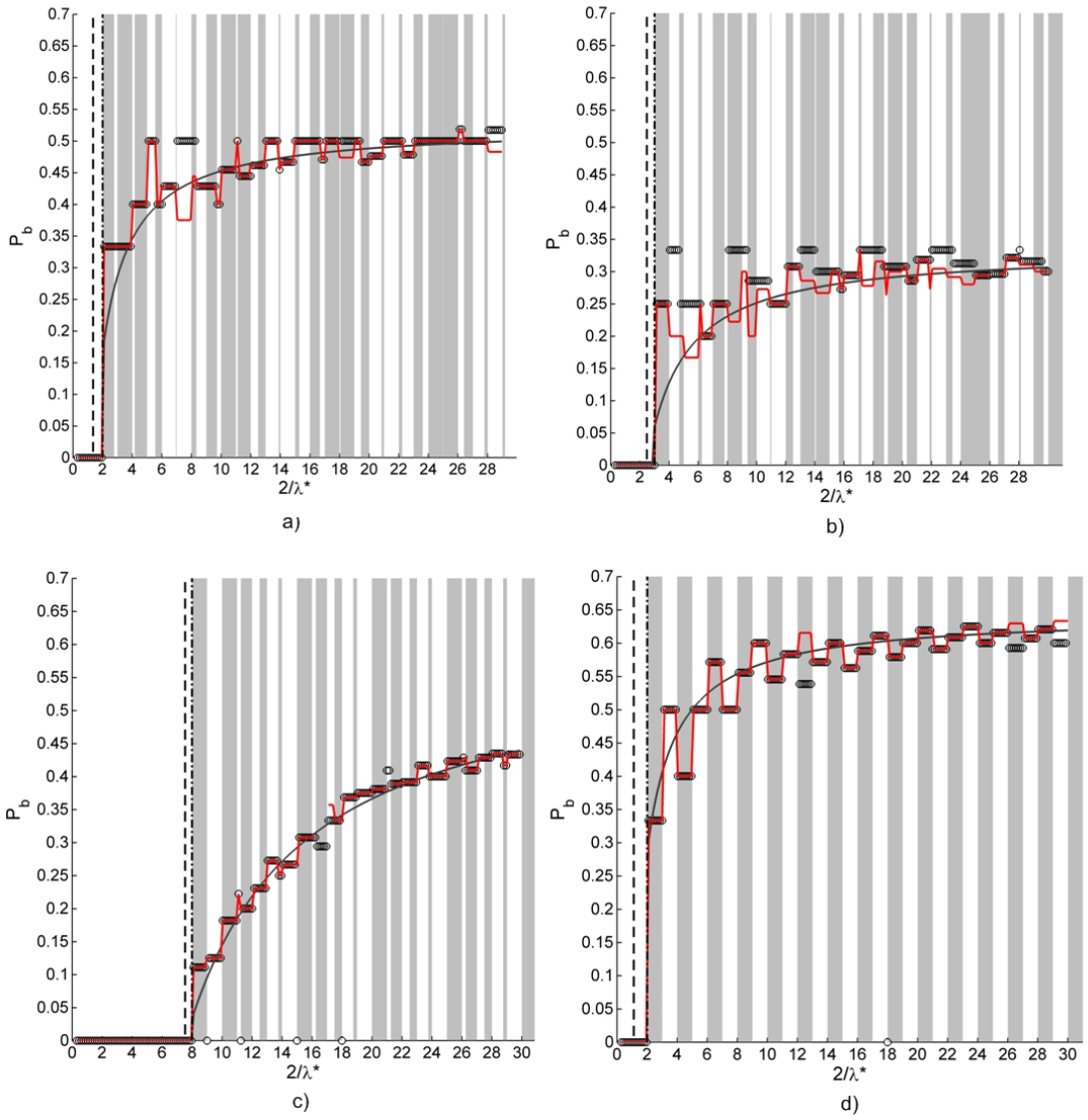

Fig S9 Fraction of droplets sorting into channel b (Pb) from the ideal-model simulations (○). The red line is the prediction by the discrete model and the solid black the continuum model.

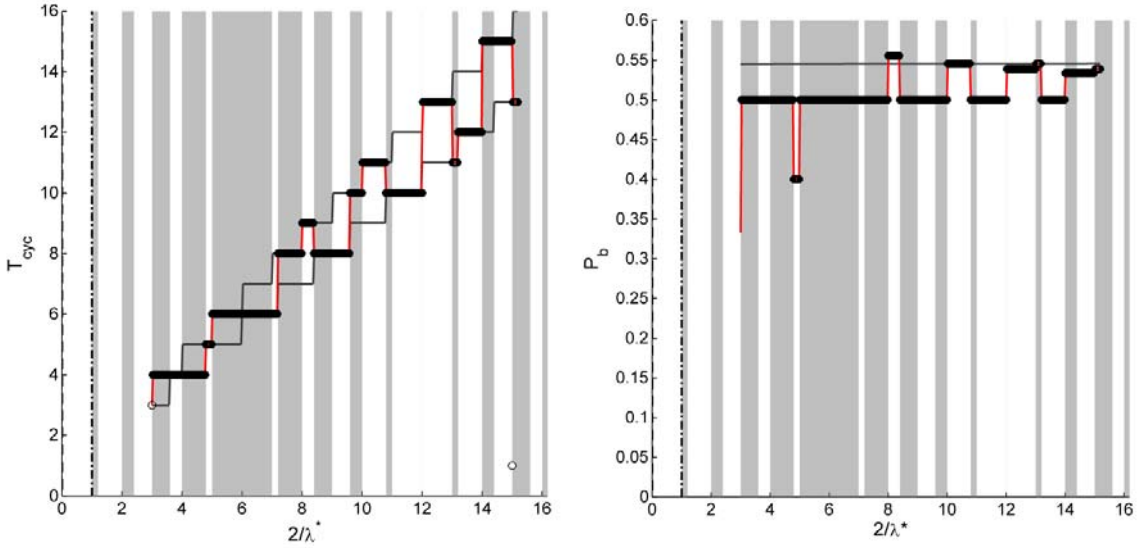

Fig.S10 Idealized numerical simulation results for the pattern length and distribution for Case 5.

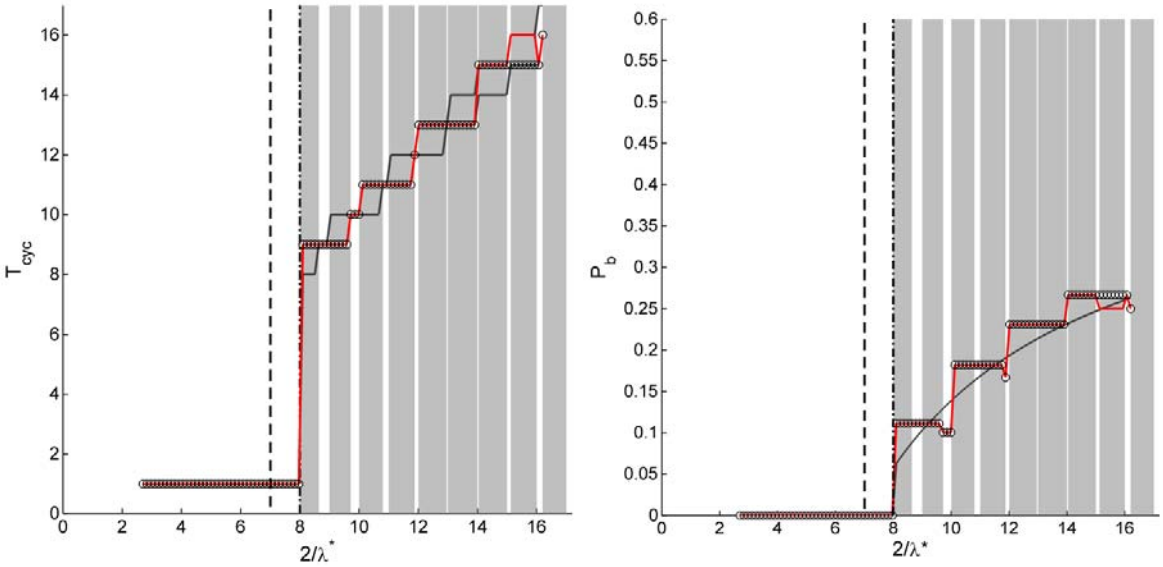

Fig.S11 Idealized numerical simulation results for the pattern length and distribution for Case 6.

S5.2 Ideal-Model Simplified Case Studies

The simplified model was tested against nine different case studies that varied the droplet resistance, branch lengths and pressures as summarized in Table S4.

Table S4 Nine case studies used to test the simplified conditions. Parameters include the length of the two branches (L_1, L_2) [mm], pressures (P_1, P_2) [Pa], and droplet equivalent lengths (L_{drop1}, L_{drop2}) [mm]. The dimensionless variables branch length ratio Λ and pressure skew P^*. Junction pressure was set to 100 Pa.

Case	L_1	L_2	P_1	P_2	L_{drop}	Λ^*	P^*
1	5	5	0	0	0.25	1	1
2	5	4.5	10	0	0.5	0.9	0.9
3	5	4	20	0	1	0.8	0.8
4	5	5	0	10	1	1	0.9
5	5	4.5	0	20	0.25	1.11	0.8
6	5	4	0	0	0.5	0.8	1
7	5	5	20	0	0.5	1	0.8
8	5	4.5	0	0	1	0.9	1
9	5	4	0	10	0.25	0.8	1.11

Figure S12 and S13 present the comparison for the pattern length and $Prob_b$ for four of these studies. Overall the same features are apparent as those already described for the general case studies. The cut-off for filtering, bifurcation between different periodic regimes, T^*_{cyc} and $Prob_b$ are all captured by the discrete model. In fact, overall the discrete model is more accurate in predicting the pattern length and droplet distribution for the simplified case studies. Across the 9 studies presented here, the model was correct in predicting the cycle time and droplet distribution 96.7% and 97.1% of time. Again mistakes in the prediction were caused by the slight over prediction of N_T near whole number values. Generally, this problem increased with greater asymmetry such as when both pressure and branch length asymmetry were combined together on the same branch. Still, the excellent accuracy of the model provides confirmation of its predictive ability.

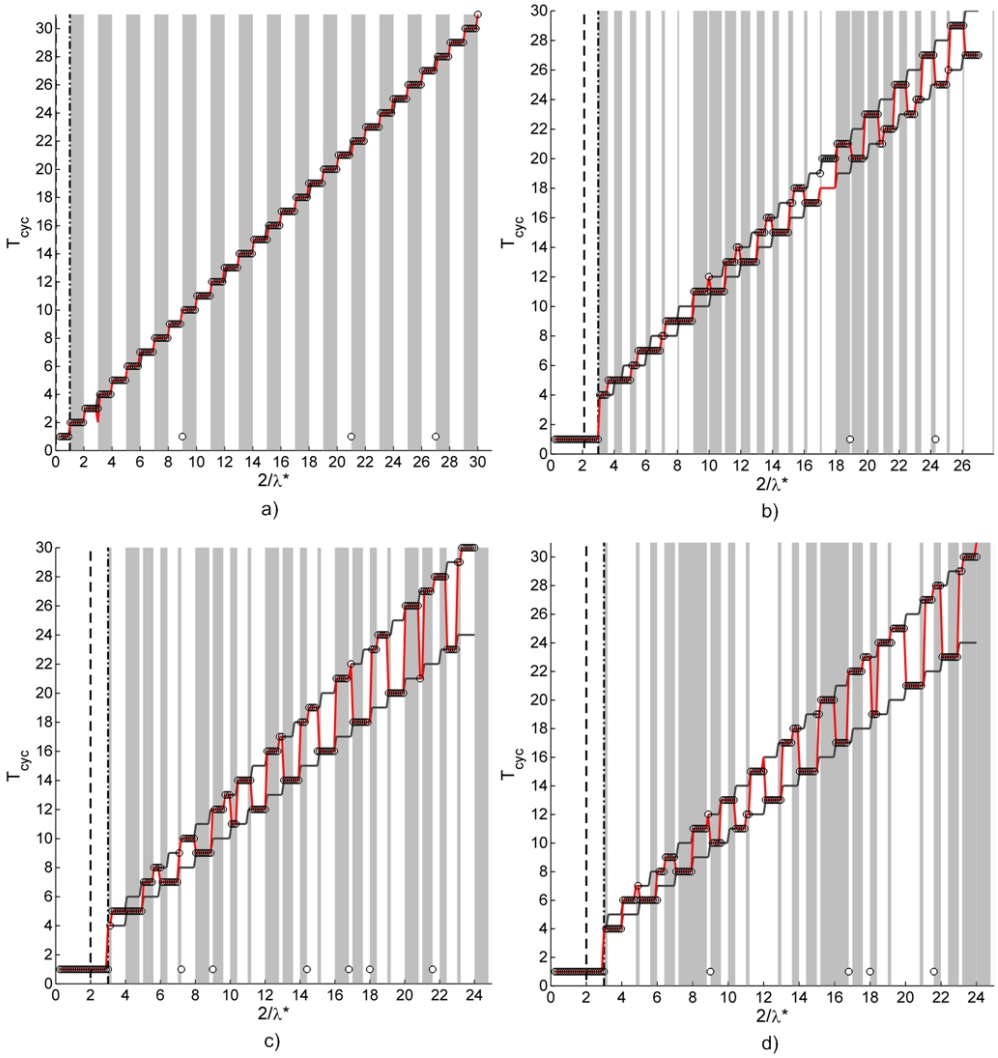

Fig.S12 Ideal-model numerical simulation results for the pattern length (○) corresponding to test Case 1 (a), Case 2 (b), Case 6 (c), and Case 9 (d) from Table S4.

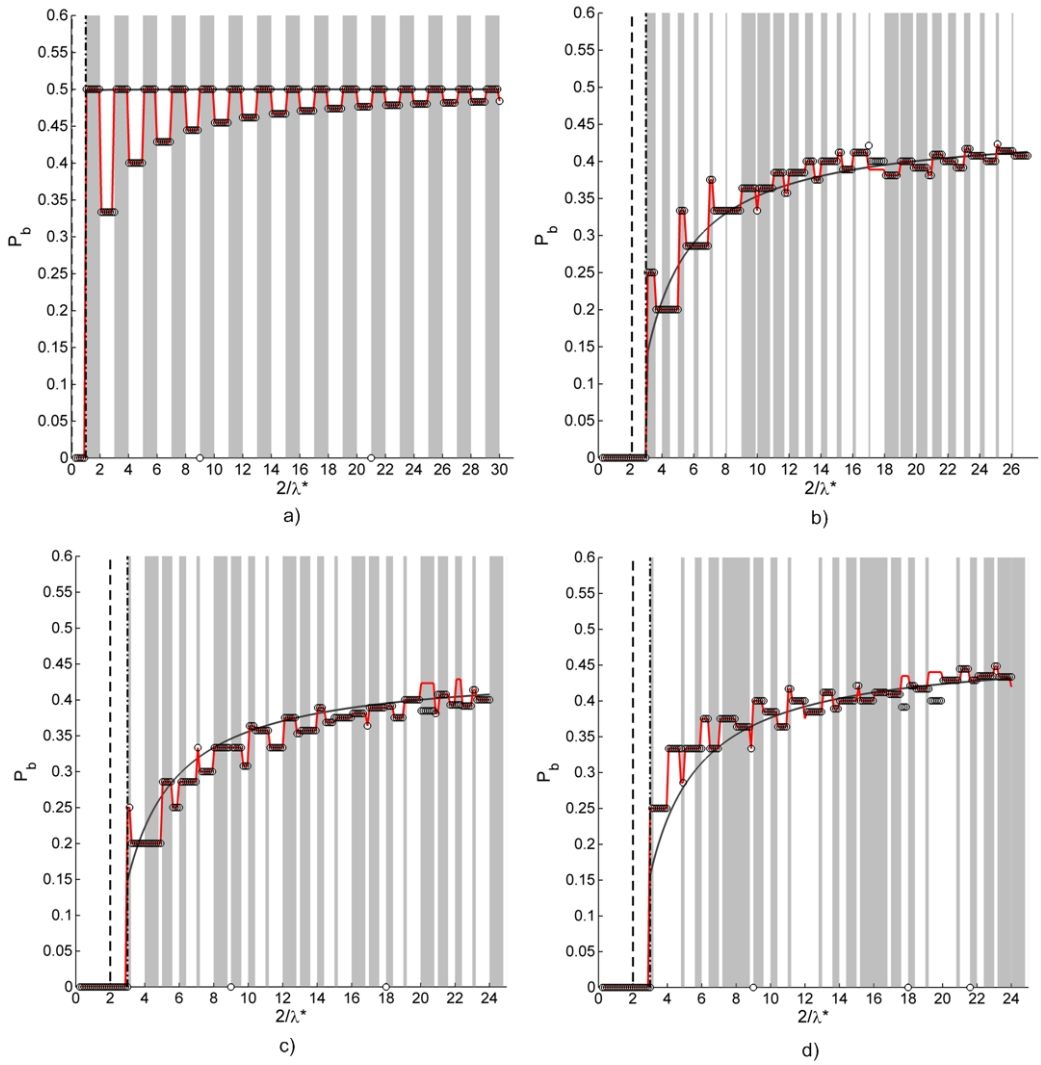

Fig.S13 Ideal-model numerical simulation results for the $Prob_b$ (○) corresponding to test Case 1 (a), Case 2 (b), Case 6 (c), and Case 9 (d).

S5.3 Full-Model Simplified Case Studies

In this section the discrete model is compared to the full-model numerical simulations. A total of 9 studies were performed as summarized in Table S5 which correspond closely to the ideal-model conditions in Table S4. The following discussion breaks down the results for a few specific cases.

Table S5 Nine case studies used to test the full-model conditions. Parameters include the length of the two branches (L_1, L_2) [mm], pressures (P_1, P_2) [Pa], and droplet equivalent lengths (L_{drop1}, L_{drop2}) [mm]. The dimensionless variables branch length ratio Λ and pressure skew P^*. Simulations were performed including the main channel inlet with the same dimensions as the experimental chip design (100 mm). Pressure at the junction was approximately 228.5 Pa and the applied pressures at the outlet were set to a base of 215 Pa.

Case	L_1	L_2	P_1	P_2	L_{drop}	Λ^*	P^*
1	5	5	0	0	1	1	1
2	5	5	0	3	0.5	1	0.821
3	5	5	0	3	0.25	1	0.821
4	5	4.5	0	0	0.5	1.11	1
5	5	4.5	3	0	0.25	1.11	0.821
6	5	4.5	0	3	1	0.9	0.821
7	5	4	0	0	0.25	0.8	1
8	5	4	3	0	1	0.8	0.821
9	5	4	0	3	0.5	0.8	0.821

Symmetric Channels, Symmetric Pressures: Case 1

Figure S14 shows the results for Case 1 where both branch lengths and pressures are symmetric. The size of the chaotic regimes grows with increasing $2/\lambda^*$ to the point where odd numbered patterns eventually disappear. For this example, the last stable odd cycle is $T^*_{cyc}=5$. Cybulski *et al.* observed a similar limit and found that the maximum odd cycle that could be observed was a function of the droplet resistance. [1] This was confirmed by repeating numerical simulations with droplet resistances of 0.5 and 0.25 mm, which produced maximum odd cycles of 11 and 19 respectively. Therefore, the trend appears to be that as the droplet resistance increases relative to the channel the stability of the system decreases.

Symmetric Channels, Asymmetric Pressures: Case 2

A comparison can be made between Case 1 and 2, where the only difference is a shift in P^* and droplet resistance. The plots for Case 2 are provided in Figure S15. Both cases have the same general pattern because the channels are symmetric and therefore the cycle times are the same. Notable differences are a shift in the critical spacing for filtering and a deviation in the distribution of droplets because of the pressure skew. Similar to Case 1, the size of the chaotic regimes increases with $2/\lambda^*$ and odd cyclical periods greater than 11 disappear.

Asymmetric Channels, Symmetric Pressures: Case 7

Figure S16 shows the results for Case 7 where the channels are asymmetric but the pressure are not. In this example, however, it is the even numbered cycle times that disappear with the maximum stable period being 12.

Asymmetric Channels, Asymmetric Pressures: Case 6

Figure S17 shows the results for Case 5 and 6 which have similar branch lengths but alternated pressures. In Case 5, the shorter channel is the filtering channel while it is the opposite for Case 6.

As expected, the selection rules developed in the manuscript are able to accurately predict the pattern length and distribution.

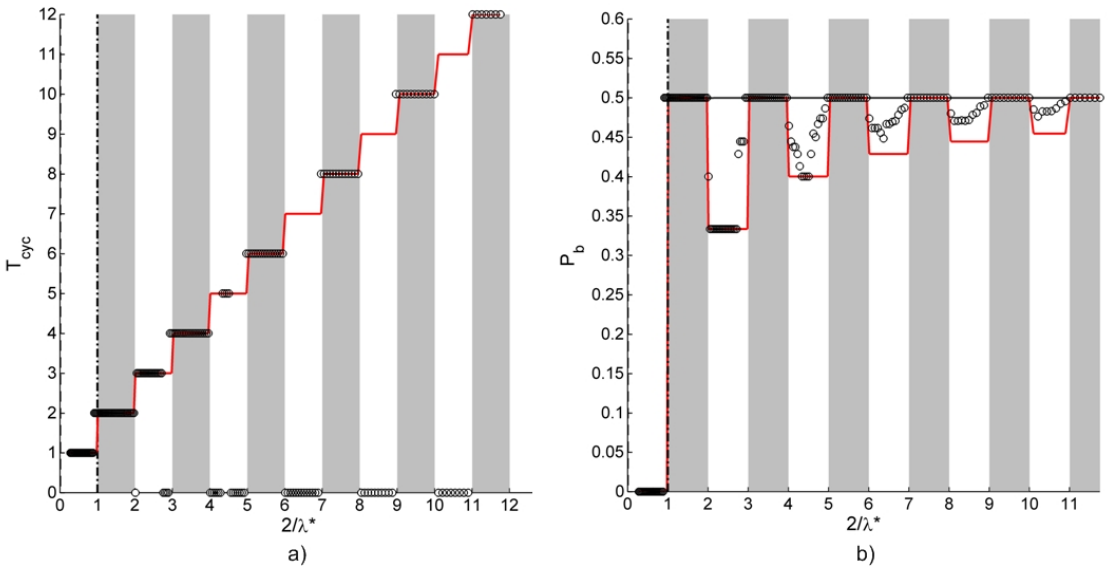

Fig.14 Full-model numerical simulation results for the T_{cyc} (a) and $Prob_b$ (b) for Case 1.

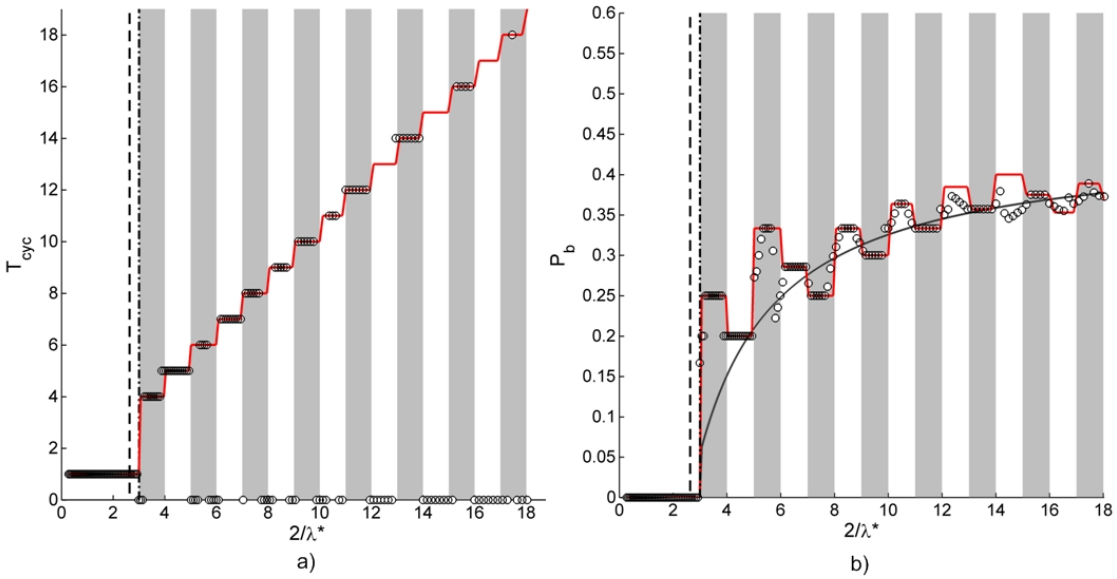

Fig.15 Full-model numerical simulation results for the T_{cyc} (a) and $Prob_b$ (b) for Case 2.

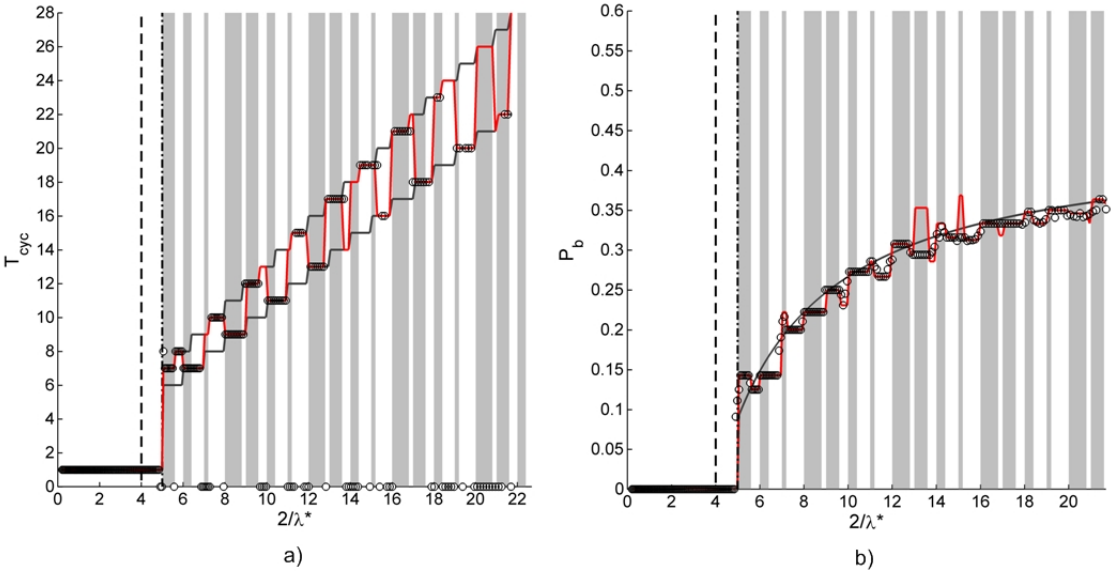

Fig.**S16** Full-model numerical simulation results for the Tcyc (a) and $Prob_b$ (b) for Case 7.

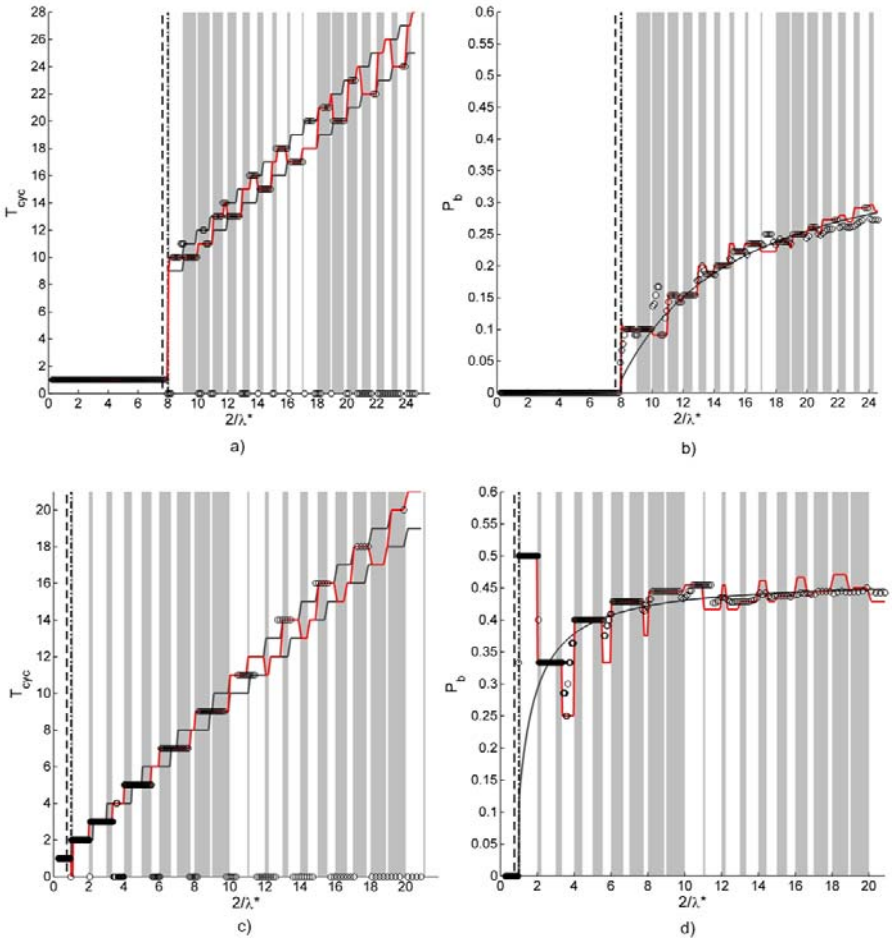

Fig.S17 Full-model numerical simulation results for the T_{cyc} (a) and $Prob_b$ (b) for Case 5 and T_{cyc} (c) and $Prob_b$ (d) for Case 6.

References

1. O. Cybulski and P. Garstecki, *Lab Chip*, 2010, **10**, 484-493.
2. D. A. Sessoms, A. Amon, et al., *Phys. Rev. Lett*, 2010, **105**, 154501.
3. B. J. Smith and D. P. Gaver, *Lab Chip*, 2010, **10**, 303-312.
4. M. J. Fuerstman, A. Lai, et al., *Lab Chip*, 2007, **7**, 1479-1489.
5. V. Labrot, M. Schindler, et al., *Biomicrofluidics*, 2009, 012804.
6. S. A. Vanapalli, A. G. Banpurkar, et al., *Lab Chip*, 2009, **9**, 982-990.